Meshfree Method for Inelastic Frame Analysis

Louie L. Yaw*, Sashi K. Kunnath* and N. Sukumar*

April 28, 2008

Abstract

The feasibility of using meshfree methods in nonlinear structural analysis is explored in an attempt to establish a new paradigm in structural engineering computation. A blended finite element and meshfree Galerkin approximation scheme is adopted to solve the inelastic response of plane frames. In the proposed method, moving least squares shape functions represent the displacement field, a plane stress approximation of the two-dimensional domain simulates beam bending, $J2$ plasticity characterizes material behavior and stabilized nodal integration yields the discrete equations. The particular case of steel frames composed of wide flange sections is investigated, though the concepts introduced can be extended to other structural materials and systems. Results of numerical simulations are compared with analytical solutions, finite element simulations and experimental data to validate the methodology. The findings indicate that meshfree methods offer an alternative approach with enhanced capabilities for nonlinear structural analysis. The proposed method can be integrated with finite elements so that a structural system is composed of mesh-free regions and finite-element regions to facilitate simulations of large-scale systems.

*Department of Civil and Environmental Engineering, University of California, Davis, CA 95616.

Introduction

Most structural engineering problems are readily solved using finite element (FE) methods, which require the discretization of the spatial domain into a collection of elements. However, FE methods encounter a host of issues in nonlinear structural analysis in applications involving cyclic and extreme loads at the limit state near collapse. Continuing research efforts to address these problems remain in the realm of FE methodology with the result that strategies applied to one class of problems may not be valid for another. The elements which make up the mesh in FE simulations must be predefined. By contrast, the discretization of a domain without resorting to a predefined mesh forms the basis of meshfree (or element-free) methods. A meshfree method typically requires only the specification of nodes (both within the domain and on the boundary) to define the domain without the need for any specific connectivity information between the nodes. Since the first formal introduction of a meshfree Galerkin method, the so-called diffuse element method by Nayroles et al. (1992), many variants of element-free approaches have been proposed by Belytschko et al. (1994), Liu et al. (1995) and Atluri and Zhu (1998) among others.

The literature on meshfree methods is vast and comprehensive. The reader is referred to overview papers by Belytschko et al. (1996), Li and Liu (2002), and Fries and Matthies (2004) for additional details on theory and applications. Most of the structural applications to date have been limited to problems in solid mechanics. With the possible exception of Weitzmann (2004) who applied meshfree methods to concrete shear walls, which are then coupled to FE beam and column line elements of a building frame structure, very little effort has been devoted toward extending meshfree methods to applications in large-scale structural engineering. In particular, collapse evaluation of frame structures is an open problem requiring large deformation analysis and inelastic material modeling. Meshfree methods are well-suited for such problems and are likely to yield new insights into such phenomenon.

Meshfree (or element-free) methods are now routinely used for many specialized applica-

tions in computational mechanics. Besides the fact that the task of accurate mesh generation in finite element methods can be time-consuming and computationally demanding (particularly for problems requiring remeshing), the growing popularity of element-free methods stems from its ability to solve certain classes of problems that are unwieldy and difficult to solve with traditional mesh-based methods. For example, large deformation problems in mesh-based (FE) methods usually require remeshing and mapping state variables to the new mesh - a process that is prone to numerical errors. In the absence of remeshing, large mesh distortions drastically reduce the solution accuracy or impede meaningful computations altogether because the Jacobian in a severely distorted element can become zero or negative. This problem is averted in meshfree methods since they are formulated to be sufficiently independent of a mesh and large distortions do not adversely affect the construction of the numerical approximation.

This work is an initial attempt to establish a new paradigm in structural engineering computation that offers a novel approach to analyzing structural engineering problems. As we move into an era of simulation-based design that seeks to design and protect the civil infrastructure from unconventional loads, there arises the need to explore and develop new tools to analyze and predict the performance of structures. Great strides have been achieved in the exploration of meshfree technology in metal forming and crashworthiness simulations, but its application in structural engineering has yet to be initiated in a decisive manner. This paper is a preliminary effort to develop a framework that allows meshfree methodology to be embedded into a finite element-based formulation (or vice-versa) and thereby enabling the simulation of large-deformation structural response to complex loads. However, prior to embarking on the ultimate challenge of tackling large-deformation structural analysis that enables modeling of complex phenomena such as fracture and separation, it is essential to demonstrate the feasibility of the method by extending well-established theories in meshfree methodology to known concepts in computational structural analysis. The following phases are envisioned to accomplish the overall goals of this research endeavor: (i) development of

a meshfree methodology for a class of structural elements and validation of the approach for nonlinear problems; (ii) extension of the developed methodology to incorporate co-rotational transformations; and (iii) incorporation of features to model material damage, separation, etc. This paper addresses only the first step in this larger effort.

Therefore, with the eventual goal of investigating the feasibility of utilizing meshfree methods in such applications, a blended finite element and meshfree Galerkin method is formulated for nonlinear analysis of planar frames. Frame bending is modeled as a 2D continuum problem under plane stress conditions. This was considered more suitable than formulating a 1D beam (as employed by Atluri et al. (1999), Donning and Liu (1997), and Suetake (2002)) because MLS shape functions would need to have cubic consistency in order to approximate both the displacement and rotation deformation fields. This causes increased difficulties in the meshfree formulation when trying to enforce displacement and slope boundary conditions. Furthermore, higher-order derivatives of the shape functions are required when solving the typical fourth-order differential equation necessary to model beam bending. Therefore, the 2D plane stress approximation was considered more suitable for the proposed formulation and future research objectives. Small strain $J2$ elasto-plasticity is used to characterize material behavior and a stabilized nodal integration scheme is employed to obtain the discrete equations. An approach to model general sections with non-uniform thickness is developed, though the particular case of steel frames composed of wide flange sections is investigated in this study. The proposed analytical scheme is applied to several examples involving beam and frame subassemblies undergoing post-elastic behavior. Results of numerical simulations are compared with analytical solutions, FE simulations and available experimental data to validate the proposed formulation.

Meshfree Moving Least Squares Shape Functions

Shape functions in meshfree methods are constructed independent of an underlying mesh structure. This is the main distinction of meshfree methods as opposed to finite element

interpolants. Moving least squares (MLS) approximants as given in Lancaster and Salkauskas (1992) are widely used in meshfree Galerkin methods (see Belytschko et al. (1996)), and a variant of MLS shape functions is used in this study. For a review of the most commonly used meshfree approximation schemes, the interested reader can refer to Sukumar and Wright (2007).

MLS Shape Function Derivation

Lancaster and Salkauskas (1992) use a weighted least squares approach to derive the MLS shape functions. The shape functions are also obtained by imposing the polynomial consistency (reproducing) conditions as given by Belytschko et al. (1996), which is the approach presented here.

In two dimensions, the moving least squares approximant for a vector-valued function $\boldsymbol{u}(\boldsymbol{x})$ is written as

$$\boldsymbol{u}^h(\boldsymbol{x}) = \sum_{a=1}^{n} \phi_a(\boldsymbol{x}) \boldsymbol{d}_a \equiv \boldsymbol{\phi}^T \boldsymbol{d}, \tag{1}$$

where $\phi_a(\boldsymbol{x})$ are the nodal shape functions, $\boldsymbol{d}_a$ is the unknown nodal coefficient, and n is the number of nodes in the neighborhood of $\boldsymbol{x}$ such that $\phi_a(\boldsymbol{x}) \neq 0$. In Belytschko et al. (1996), the MLS shape function $\phi_a(\boldsymbol{x})$ is assumed to be of the form

$$\phi_a(\boldsymbol{x}) = \boldsymbol{P}^T(\boldsymbol{x}_a) \boldsymbol{\alpha}(\boldsymbol{x}) w(\boldsymbol{x}_a), \tag{2}$$

where $\boldsymbol{P}(\boldsymbol{x}) = \{1 \; x \; y\}^T$ is a linear basis in two dimensions, $\boldsymbol{\alpha}(\boldsymbol{x})$ is a vector of unknowns to be determined and $w(\boldsymbol{x}) \geq 0$ is a weighting function.

The vector of unknowns, $\boldsymbol{\alpha}(\boldsymbol{x})$, is determined by imposing the consistency (reproducing) condition, i.e., the shape function must exactly reproduce $\boldsymbol{P}(\boldsymbol{x})$. Hence, ϕ_a must satisfy

$$\boldsymbol{P}(\boldsymbol{x}) = \sum_{a=1}^{n} \boldsymbol{P}(\boldsymbol{x}_a) \phi_a(\boldsymbol{x}). \tag{3}$$

Now, substituting Eq. (2) into Eq. (3) yields

$$\boldsymbol{P}(\boldsymbol{x}) = \Big[\sum_{a=1}^{n} \boldsymbol{P}(\boldsymbol{x}_a)\boldsymbol{P}^T(\boldsymbol{x}_a)w(\boldsymbol{x}_a)\Big]\boldsymbol{\alpha}(\boldsymbol{x}) = \boldsymbol{A}(\boldsymbol{x})\boldsymbol{\alpha}(\boldsymbol{x}), \tag{4}$$

which gives

$$\boldsymbol{\alpha}(\boldsymbol{x}) = \boldsymbol{A}^{-1}(\boldsymbol{x})\boldsymbol{P}(\boldsymbol{x}). \tag{5}$$

Upon substitution of $\boldsymbol{\alpha}(\boldsymbol{x})$ in Eq. (2) the final shape function expression is

$$\phi_a(\boldsymbol{x}) = \boldsymbol{P}^T(\boldsymbol{x}_a)\boldsymbol{A}^{-1}(\boldsymbol{x})\boldsymbol{P}(\boldsymbol{x})w(\boldsymbol{x}_a). \tag{6}$$

The weight function provides the local character of the shape function. For example, the shape function ϕ_a has a radius of support, ρ_a, within which it is nonzero. This is best illustrated in one dimension (see Fig. 1), where the following quartic weight function is used to generate the shape functions:

$$w(q) = \begin{cases} 1 - 6q^2 + 8q^3 - 3q^4 & q \leq 1 \\ 0 & q > 1 \end{cases}, \tag{7}$$

where $q = \|\boldsymbol{x} - \boldsymbol{x}_a\|/\rho_a$. Note that the shape functions do not interpolate on the boundary ($\phi_a(\boldsymbol{x}_b) \neq \delta_{ab}$). This characteristic makes it difficult to impose essential boundary conditions.

Integrating the Weak Form

The variational (weak) form arises by taking the first variation of the potential energy and setting it to zero. Using the strain-displacement relation ($\boldsymbol{\varepsilon} = \boldsymbol{B}\boldsymbol{d}$) and the displacement approximation Eq. (1) in the weak form leads to

$$\boldsymbol{f}^{ext} - \boldsymbol{f}^{int} = \boldsymbol{0}, \tag{8}$$

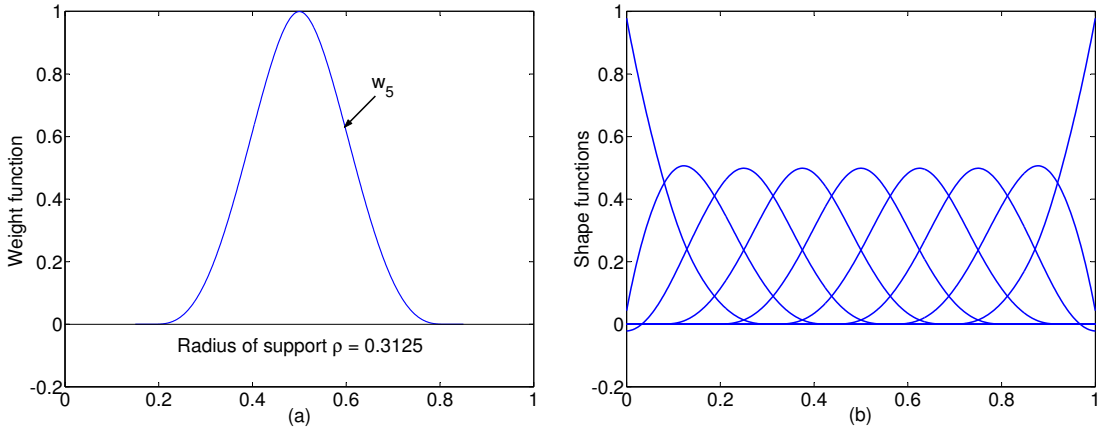

Figure 1: MLS construction (9 equi-spaced nodes): (a) Weight function, (b) Shape functions

where

$$\boldsymbol{f}^{ext} = \int_S \boldsymbol{\phi}^T \bar{\boldsymbol{t}}\, dS, \quad \boldsymbol{f}^{int} = \int_V \boldsymbol{B}^T \boldsymbol{\sigma}\, dV, \tag{9}$$

$\boldsymbol{\sigma}$ is the Cauchy stress and $\bar{\boldsymbol{t}}$ is the prescribed traction vector. For a linear elastic material, constitutive relations ($\boldsymbol{\sigma} = \boldsymbol{C\varepsilon} = \boldsymbol{CBd}$) are substituted in Eq. (8) to give

$$\boldsymbol{Kd} = \boldsymbol{f}^{ext}, \tag{10}$$

where the stiffness matrix is

$$\boldsymbol{K} = \int_V \boldsymbol{B}^T \boldsymbol{CB}\, dV. \tag{11}$$

For plane stress, the elastic modulus matrix, $\boldsymbol{C}$, is

$$\boldsymbol{C} = \frac{E}{1-\nu^2} \begin{bmatrix} 1 & \nu & 0 \\ \nu & 1 & 0 \\ 0 & 0 & \frac{1-\nu}{2} \end{bmatrix}, \tag{12}$$

where E is the modulus of elasticity and ν is Poisson's ratio.

In an effort to depart from using elements for the purpose of numerical integration, a node-based integration technique is used to compute $\boldsymbol{K}$ in Eq. (11). For node-based

integration, a background geometric structure, such as a Voronoi diagram, is still required. This geometric structure is preferable since it is node-based rather than element-based and no Jacobian is required. A further advantage of nodal integration is that state variables, such as material properties, are associated with nodes rather than elements. The nodal integration procedure adopted here closely follows the integration scheme proposed by Chen et al. (2001).

Consider the Voronoi cell domain V_a and boundary of segments S_a enclosing node a as shown in Fig. 2. Over the domain V_a, the components of the smoothed strain tensor (finite volume averaging) are

$$\varepsilon_{ij}(\boldsymbol{x}_a) = \frac{1}{2A_a}\int_{V_a}(u_{i,j}+u_{j,i})\,dV = \frac{1}{2A_a}\int_{S_a}(u_i n_j + u_j n_i)\,dS, \tag{13}$$

where the last expression is found by using the divergence theorem, A_a is the Voronoi cell area associated with node a, and n_i is the ith component of a unit vector normal to the Voronoi cell boundary S_a. Now, similar to FEM, $\boldsymbol{\varepsilon}$ of Eq. (13) is written as a strain-displacement

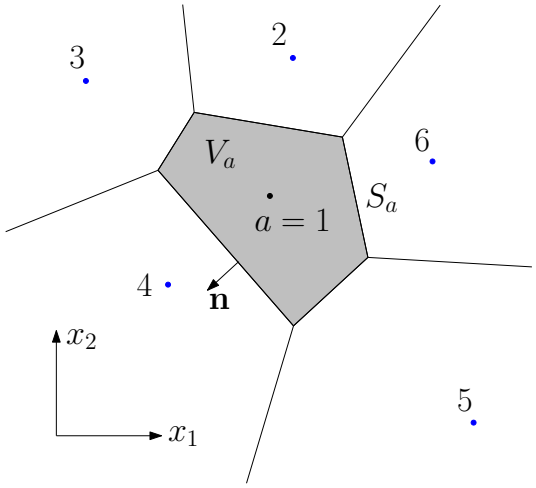

Figure 2: Voronoi cell of node a.

relation. Using Eq. (1) in Eq. (13) and defining some new variables the strain-displacement

relations are

$$\boldsymbol{\varepsilon}(\boldsymbol{x}_a) = \sum_{b=1}^{6} \boldsymbol{B}_b(\boldsymbol{x}_a)\boldsymbol{d}_b = [\mathbf{B}_1\ \mathbf{B}_2 \cdots \mathbf{B}_6] \begin{bmatrix} \mathbf{d}_1 \\ \mathbf{d}_2 \\ \vdots \\ \mathbf{d}_6 \end{bmatrix} \equiv \mathbf{B}\mathbf{d}, \tag{14}$$

where the index b ranges over the nodes whose associated shape function supports cover any vertex of the Voronoi cell a (i.e., nodes 1 to 6 for the example of Fig. 2) and the following definitions apply:

$$\boldsymbol{\varepsilon} = [\varepsilon_{11}\ \varepsilon_{22}\ 2\varepsilon_{12}]^T \quad \text{and} \quad \boldsymbol{d}_a = [d_{a1}\ d_{a2}]^T \tag{15}$$

$$\boldsymbol{B}_b(\boldsymbol{x}_a) = \begin{bmatrix} b_{b1}(\boldsymbol{x}_a) & 0 \\ 0 & b_{b2}(\boldsymbol{x}_a) \\ b_{b2}(\boldsymbol{x}_a) & b_{b1}(\boldsymbol{x}_a) \end{bmatrix} \tag{16}$$

$$b_{bi}(\boldsymbol{x}_a) = \frac{1}{A_a} \int_{S_a} \phi_b(\boldsymbol{x}) n_i(\boldsymbol{x})\, dS. \tag{17}$$

On using the strain-displacement relation Eq. (14) in Eq. (11) gives $\boldsymbol{K}$ as

$$\boldsymbol{K}_{bc} = \sum_{a=1}^{n} \boldsymbol{B}_b^T(\boldsymbol{x}_a)\boldsymbol{C}\boldsymbol{B}_c(\boldsymbol{x}_a)A_a t. \tag{18}$$

Note that in the above expression the indices b and c range over node numbers associated with node a (see Eq. (14)) and the thickness of the two dimensional domain, t, is generally taken as unity. The external force vector $\boldsymbol{f}^{ext}$ of Eq. (9) is found similarly (see Chen et al. (2001)).

Enforcement of Essential Boundary Conditions

In general MLS shape functions do not possess the Kronecker-delta property. Hence it is difficult to enforce essential boundary conditions when using MLS shape functions. To overcome this problem a variety of techniques have been devised to enforce essential boundary conditions such as Lagrange multiplier method, penalty method, Nitsche's method and con-

tinuous blending method (Fernández-Méndez and Huerta (2004)). In this study, continuous blending is used because it allows the MLS shape functions to blend into FE shape function regions. Hence, the MLS shape functions are used everywhere except at nodes where essential boundary conditions need to be enforced. At such nodes FE shape functions are used, and enforcement of essential boundary conditions is imposed on the finite element nodes in the standard way. Continuous blending as proposed by Huerta and Fernández-Méndez (2004) is

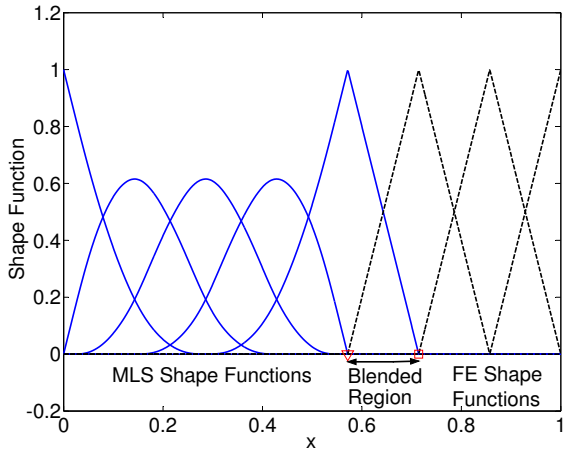

Figure 3: Blending of linear MLS and FE shape functions.

accomplished by recognizing three distinct regions possible in the discretized domain when the two types of shape functions are used. These regions are (i) MLS regions, (ii) blended regions (transition between MLS and FE shape functions) and (iii) FE regions. For region (i) the MLS shape functions are as given in Eq. (6). In this work, a linear polynomial basis is used to construct the MLS shape functions. The finite element shape functions perform the best in the method of continuous blending if they are also linear as indicated in Huerta and Fernández-Méndez (2004). Therefore in region (ii) the MLS shape functions are blended into linear quadrilateral finite element shape functions. Lastly, in region (iii) the transition is complete and typical linear quadrilateral finite elements are solely used to construct the approximate solution.

The meshfree approximation in a blended region is represented as

$$\boldsymbol{u}^h(\boldsymbol{x}) = \sum_{a=1}^{n_{MLS}} \tilde{\phi}_a(\boldsymbol{x})\boldsymbol{d}_a + \sum_{b=1}^{n_{FE}} N_b(\boldsymbol{x})\boldsymbol{u}_b, \tag{19}$$

where the tilde is used to denote the blended approximation. If a node needs enforcement of an essential boundary condition there is a two dimensional linear finite element shape function, N_b, associated with the node. Note that a blended region does not have a complete set of finite element shape functions. Hence, in Eq. (19) the sum over a is for all MLS shape functions that are nonzero in the given blended region and the sum over b is for all nonzero FE shape functions. The MLS shape functions in a blended region are constructed the same as done previously by enforcing the consistency condition:

$$\mathbf{P}(\boldsymbol{x}) = \sum_{a=1}^{n_{MLS}} \tilde{\phi}_a(\boldsymbol{x})\mathbf{P}(\boldsymbol{x}_a) + \sum_{b=1}^{n_{FE}} N_b(\boldsymbol{x})\mathbf{P}(\boldsymbol{x}_b). \tag{20}$$

Equation (20) states that in the blended region the combined FE and MLS approximation Eq. (19) is consistent with the polynomial that it is trying to approximate. Then, following a procedure similar to the MLS shape function derivation, the MLS approximant in the blended region is

$$\tilde{\phi}_a(\boldsymbol{x}) = \phi_a(\boldsymbol{x}) - \mathbf{P}^T(\boldsymbol{x}_a)\mathbf{A}^{-1}\left(\sum_{b=1}^{n_{FE}} N_b(\boldsymbol{x})\mathbf{P}(\boldsymbol{x}_b)\right)w(\boldsymbol{x}_a). \tag{21}$$

The first term on the right hand side of Eq. (21) is the MLS shape function of node a in the meshfree region. The second term on the right hand side of Eq. (21) is the correction to the MLS shape function of node a if it is nonzero in the blended region. An example of one-dimensional linear MLS shape functions blended into linear finite elements is shown in Fig. 3.

Numerical Implementation

Several issues in the numerical implementation require further attention. First, it is shown

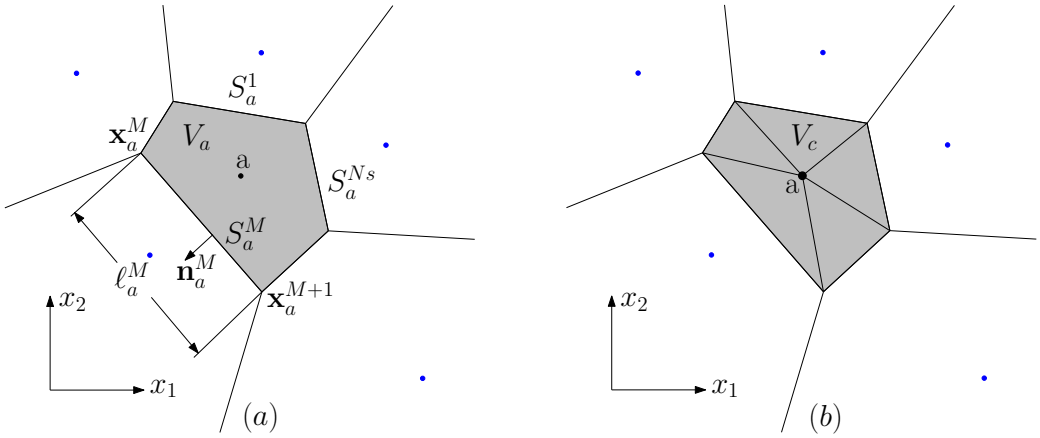

Figure 4: (a) Integration over Voronoi cell, (b) Triangular subcells

how to calculate the individual components of the smoothed strain-displacement matrices. Secondly, nodal integration is unstable and requires some form of numerical stabilization, which is addressed. Here, the terms stable and stabilization are not a mathematically precise usage; however, they are often used in this context in the meshfree literature.

Numerical Evaluation of Strain-Displacement Matrix Components

To carry out the integration, by numerically evaluating the components Eq. (17) of the strain-displacement matrix, a two-node trapezoidal rule is employed. As indicated in the example of Fig. 4(a), $\boldsymbol{x}_a^M$ and $\boldsymbol{x}_a^{M+1}$ are the end nodes of segment S_a^M. The length of the segment is ℓ_a^M and surface normal of the segment is $\boldsymbol{n}_a^M$. Using these definitions Eq. (17) is rewritten as a summation over the number of Voronoi cell segments, N_s,

$$b_{bi}(\boldsymbol{x}_a) = \frac{1}{A_a}\sum_{M=1}^{N_s}\left[\phi_b(\boldsymbol{x}_a^M)n_{ai}^M\frac{\ell_a^M}{2} + \phi_b(\boldsymbol{x}_a^{M+1})n_{ai}^M\frac{\ell_a^M}{2}\right]. \tag{22}$$

When the last segment in the summation is reached define $M+1 = N_s+1 \equiv 1$. Next, noting that Eq. (22) only involves evaluation of $\phi_b n_{ai}$ at the vertices of the Voronoi cell for node a, Eq. (22) is now written as

$$b_{bi}(\boldsymbol{x}_a) = \frac{1}{A_a}\sum_{M=1}^{N_s}\left[\frac{1}{2}(n_{ai}^M\ell_a^M + n_{ai}^{M+1}\ell_a^{M+1})\phi_b(\boldsymbol{x}_a^{M+1})\right]. \tag{23}$$

This last equation involves no derivatives of the MLS shape functions. The technique of nodal integration is used in linear problems (Chen et al. 2001) and also in nonlinear problems involving large displacements (Chen et al. 2002).

Stabilization of Stiffness Matrix

Nodal integration instabilities are often manifested by hourglass modes in the calculated deflected shape, by spurious low-energy modes in an eigen analysis and by locking in nearly or totally incompressible materials. Hence, some form of stabilization is needed for the stiffness matrix given in Eq. (18). Puso et al. (2008) proposed the following stabilization scheme:

$$\boldsymbol{K}^s = \boldsymbol{K}_{bc} + \sum_{a=1}^{n} \left[\alpha_s \sum_{c \in T_a} (\boldsymbol{B}(\boldsymbol{x}_a) - \boldsymbol{B}^c(\boldsymbol{x}_a))^T \boldsymbol{C}_s (\boldsymbol{B}(\boldsymbol{x}_a) - \boldsymbol{B}^c(\boldsymbol{x}_a)) A_c t \right], \tag{24}$$

where $\boldsymbol{K}^s$ is the stabilized matrix, $\alpha_s = 1.0$ is the stabilization factor and $\boldsymbol{C}_s$ is the stabilization modulus matrix. The first term in the summation of Eq. (24) is equivalent to Eq. (18) and for each node a the second term is a summation over the set of triangular subcells, T_a, for Voronoi cell a (see Fig. 4(b)). Over each triangular subcell c the $\boldsymbol{B}^c$ matrix is constructed in the same way that $\boldsymbol{B}$ matrices are constructed over a Voronoi cell.

When constructing $\boldsymbol{C}_s$ for plastic materials with Lamé parameters μ and λ, the recommendation of Puso et al. (2008) is adopted such that the effective moduli are

$$\tilde{\mu} = H/2 \quad \text{and} \quad \tilde{\lambda} = \max(\lambda, 12.5H), \tag{25}$$

where for linear hardening, H is the hardening modulus and for exponential hardening, H is taken as the slope of the tangent to the exponential hardening curve at zero plastic strain. The effective elastic modulus $\tilde{E}$ and Poisson's ratio $\tilde{\nu}$ in terms of $\tilde{\mu}$ and $\tilde{\lambda}$ are given by

$$\tilde{E} = \frac{\tilde{\mu}(3\tilde{\lambda} + 2\tilde{\mu})}{\tilde{\lambda} + \tilde{\mu}} \quad \text{and} \quad \tilde{\nu} = \frac{\tilde{\lambda}}{2(\tilde{\lambda} + \tilde{\mu})}. \tag{26}$$

Summary of Discrete Equations

In general Eq. (8) is nonlinear since the unknown stress field at time $n+1$ is a nonlinear function of strain. Hence, following an approach similar to that presented in finite element monographs such as Gosz (2006), linearization of $\boldsymbol{\sigma}$ gives

$$\boldsymbol{\sigma}_{n+1} \approx \boldsymbol{\sigma}_n + \boldsymbol{C}_n^{ep} \Delta \boldsymbol{\varepsilon}_n = \boldsymbol{\sigma}_n + \boldsymbol{C}_n^{ep} \boldsymbol{B} \Delta \boldsymbol{d}_n, \tag{27}$$

where $\Delta \boldsymbol{d}_n = \boldsymbol{d}_{n+1} - \boldsymbol{d}_n$ and $\boldsymbol{C}_n^{ep}$ is the plane stress elasto-plastic tangent modulus matrix (Simo and Taylor (1986)) and use has been made of the strain-displacement relations. Substitution of Eq. (27) into Eq. (8) gives

$$\int_V \boldsymbol{B}^T \boldsymbol{C}_n^{ep} \boldsymbol{B} \, dV \Delta \boldsymbol{d}_n = \left\{ \int_S \boldsymbol{\phi}^T \bar{\boldsymbol{t}} \, dS \right\}_{n+1} - \int_V \boldsymbol{B}^T \boldsymbol{\sigma}_n \, dV \quad \Rightarrow \quad \boldsymbol{K}_n^t \Delta \boldsymbol{d}_n = \boldsymbol{f}_{n+1}^{ext} - \boldsymbol{f}_n^{int}, \tag{28}$$

where $\boldsymbol{K}_n^t$ is the tangent stiffness matrix. A Newton-Raphson scheme is used to iterate the linearized (see Gosz (2006)) system of Eqs. (28) until convergence is achieved. The iterated equation is written as

$$\boldsymbol{K}_{n+1}^{t(\nu)} \Delta \boldsymbol{d}_n^{(\nu)} = \boldsymbol{f}_{n+1}^{ext} - \boldsymbol{f}_{n+1}^{int(\nu)}, \tag{29}$$

where ν is the iteration counter. It is understood that when the iteration counter is zero the matrices and vectors are evaluated at time n, i.e., $\boldsymbol{f}_{n+1}^{int(0)} = \boldsymbol{f}_n^{int}$, etc.

On the basis of the preceding developments, the discrete equations are obtained as follows:

$$\boldsymbol{K}_{bc} = \sum_{a=1}^{n} \boldsymbol{B}_b^T(\boldsymbol{x}_a) \tilde{\boldsymbol{C}} \boldsymbol{B}_c^T(\boldsymbol{x}_a) A_a t \tag{30a}$$

$$\boldsymbol{K}^s = \boldsymbol{K}_{bc} + \sum_{a=1}^{n} \left[\alpha_s \sum_{c \in T_a} (\boldsymbol{B}(\boldsymbol{x}_a) - \boldsymbol{B}^c(\boldsymbol{x}_a))^T \boldsymbol{C}_s (\boldsymbol{B}(\boldsymbol{x}_a) - \boldsymbol{B}^c(\boldsymbol{x}_a)) A_c t \right] \tag{30b}$$

$$\boldsymbol{f}_b^{ext} = \sum_{a=1}^{n_b} \phi_b(\boldsymbol{x}_a) \bar{\boldsymbol{t}}(\boldsymbol{x}_a) S_a. \tag{30c}$$

In the above equations, for nonlinear problems, such as elasto-plasticity, $\tilde{\boldsymbol{C}} = \boldsymbol{C}^{ep}$ and $\boldsymbol{K}^s$ is the stabilized tangent stiffness matrix to be used in Eq. (29). For linear problems $\tilde{\boldsymbol{C}}$ is replaced with Eq. (12) and the stabilized stiffness matrix, $\boldsymbol{K}^s$, replaces $\boldsymbol{K}$ in Eq. (10). In Eq. (30c) S_a is the length along the boundary of the Voronoi cell of node a along which the traction $\bar{\boldsymbol{t}}$ acts, and n_b is the number of boundary points. Once the discrete equations are solved for the unknown $\boldsymbol{d}$ values the displacements at each node are found by using Eq. (1). The strains at each node a are found by using Eq. (14) and stresses are found by using the appropriate constitutive relations.

Formulation for Sections with Non-uniform Thickness

In order to allow for non-uniform thickness Eq. (30a) is modified to allow a unique thickness, t_a, for each node a:

$$\boldsymbol{K}_{bc} = \sum_{a=1}^{n} \boldsymbol{B}_b^T(\boldsymbol{x}_a)\tilde{\boldsymbol{C}}\boldsymbol{B}_c^T(\boldsymbol{x}_a)A_a t_a. \tag{31}$$

A similar modification will be required for Eq. (30b). By setting the thickness for different regions of the 2D continuum it is possible to model a variety of common beam cross-sections. For example, I-beams and channels in the case of steel cross-sections or T-beams and I shaped girders in the case of concrete. Of course the thicknesses are set to obtain a moment of inertia which matches the beam being modeled. The validation problems included below are for beams of I shaped cross-section. Therefore, in Appendix A an example is provided which illustrates the process of deriving the thickness of a section associated with a particular meshfree node to obtain the correct moment of inertia for an I-beam.

Validation of Methodology

The linear and nonlinear response of several realistic frame subassemblies are evaluated using the proposed blended FEM and meshfree method. For all example problems only constrained nodes have FE shape functions for enforcement of essential boundary conditions by the blending method. The remaining domain is modeled with MLS shape functions.

The results are compared to analytical solutions in the case of the cantilever beam and to experimental data for a frame corner connection and a portal frame. Also included are comparisons with simulations using one-dimensional fiber-section beam elements since they are commonly employed in nonlinear frame analysis. The open-source structural analysis software OpenSees (Mazzoni et al. 2007) is used for both the 1D fiber beam (*dispBeamColumn* element) simulations and the FE simulations with enhanced strain quadrilateral elements.

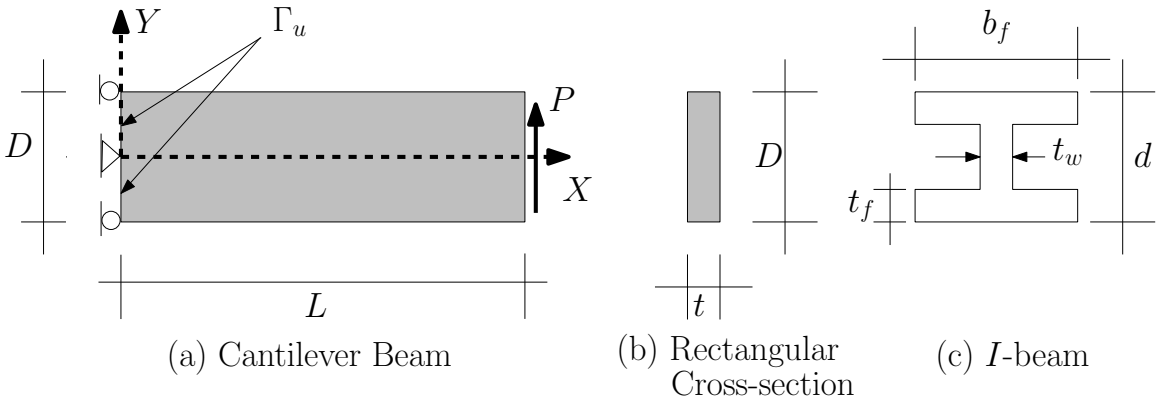

Figure 5: Cantilever beam.

Cantilever Beam

First, the results for an I-beam cantilever using a linear elastic material are presented. In Table 1, with grid refinement, the normalized tip displacement and bending stress values asymptotically approach 1.0 where $\delta_{\text{theor.}} = 0.0308$ in and $\sigma_{\text{theor.}} = 25.0$ ksi. For these results the variables used are $E = 29,000$ ksi, $\nu = 0.3$, $P = 5$ kips, $L = 10$ in, $I_{xx} = 2.0$ in^4, $d = 2$ in, $t_w = 1$ in with t_f and b_f dependent on the grid as explained in Appendix A. Secondly, the results for an I-beam cantilever using an elasto-plastic material model are shown in Fig. 6. This analysis is performed with small strain plane stress $J2$ elasto-plasticity as outlined in Simo and Taylor (1986). The solution procedure uses Newton-Raphson iterations at the global level to enforce equilibrium between internal and external forces (Gosz 2006), and at the constitutive level an implicit integration scheme with radial return is employed (Simo

Table 1: Cantilever I-beam tip displacement and maximum bending stress.

Grid	$\delta/\delta_{\text{theor.}}$ (in)	$\sigma_{xx}/\sigma_{\text{theor.}}$ (ksi)
11×3	1.045	0.77
21×5	1.025	0.89
31×7	1.016	0.94
41×9	1.012	0.95
51×11	1.010	0.96
61×13	1.009	0.97

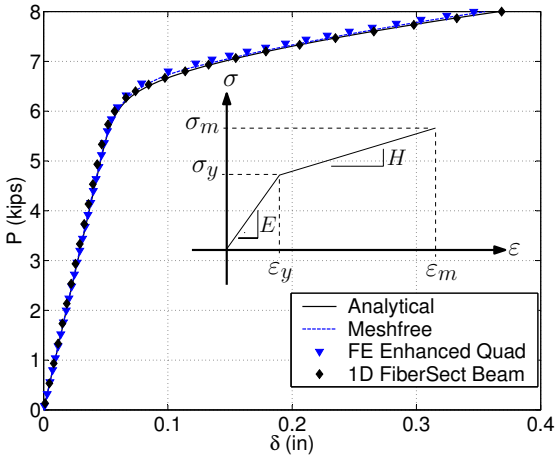

Figure 6: Inelastic response of cantilever I-beam.

and Hughes 1998). In Fig. 6, the load versus displacement response is compared to an analytical solution for an elasto-plastic cantilever based on Euler-Bernoulli beam theory with an elastic shear deformation term included similar to Eq. (37). For the results of Fig. 6, $I_{xx} = 1.313$ in^4, however, all remaining geometry and material properties are the same as the linear analysis. In addition, the hardening modulus is $H = 500$ ksi, the yield stress is 36 ksi, and the maximum applied load is 8 kips. The I-beam is modeled with a 51 by 11 grid of nodes (similar to 500 elements). Figure 6 also shows results for a 1D fibersection beam model with a discretization of 10 finite beam elements and a 2D continuum model using 500 enhanced strain quadrilateral finite elements.

The analytical solution uses the bilinear model shown within Fig. 6 and is developed independently of previous work. However, the initial steps to find the analytical solution are

similar to Yu and Zhang (1996) who set out preliminary formulas for an elasto-plastic beam of rectangular cross-section with a linear hardening material. The interested reader is also referred to Phillips (1956), where a method to express the curvature as a function of applied moment is presented for beams of various cross-sections, including a plastically deforming I-beam. Once curvature is known at every cross-section deflection is calculated using the Second Area Moment theorem.

The numerical solution differs from the analytical solution for a variety of reasons. First, the discretization of the cantilever across the beam depth cannot exactly represent the bi-linear stress profile. Secondly, the analytical solution assumes plane sections remain plane. However, the numerical solution is based on the elasticity solution which does not restrict plane sections to remain planar. Thirdly, the exact displacement boundary conditions for an I-beam are not known. Hence, all nodes at the support are pinned. Lastly, the analytical solution is based on the bilinear material model within Euler-Bernoulli beam theory. This differs from the numerical solution where a $J2$ elasto-plastic material model in plane stress is assumed. Despite these differences, the agreement between the numerical and analytical results is excellent.

Frame Corner Connection

In the second example, the nonlinear response of a frame corner connection tested to failure by Beedle and Christopher (1964) is investigated and the computed response is compared with experimental results. The frame connection is made of W30x108 members and stiffeners. In the numerical model larger thicknesses are specified along straight and diagonal stiffener lines to properly simulate the effect of the stiffeners on the response of the connection. The resulting experimental versus simulated load displacement results are shown in Fig. 7. Load displacement results are also shown for 1D fibersection beam models with a discretization of 22 finite beam elements. For the beam elements, in one case the panel zone elements were allowed to have an elasto-plastic response, whereas the other case was forced

to have an elastic panel zone. The numerical results vary from the experimental results for several reasons. First, Beedle and Christopher (1964) do not provide the material properties for the corner connection material. Theoretical predictions for the load displacement curve based on an elastic perfectly plastic material provided by Beedle and Christopher (1964) indicate their assumed yield stress value of 36 ksi. However, following the recommendation of Johnston et al. (1953), for a more accurate plastic analysis, a yield plateau value of 33 ksi is used in the material model herein. Secondly, the hardening used for the numerical results is based on an assumed ultimate value of 55 ksi. Beedle and Christopher (1964) mention that the frame connection did develop its full plastic moment but failed by flange local buckling and that this accounts for some hardening followed by softening as shown by the experimental curve. Hence, it is not reasonable to expect that the estimated hardening behavior provided in the numerical results (which does not consider flange local buckling) will exactly match the experimental results. Despite these differences, the numerical results are in general agreement with the experimental results. Figure 8 shows an example of the final (160 kip load) stresses for the corner connection. The σ_{xx} stresses are oriented along the axis of the top W30x108 beam. It is evident from the stress plot that a plastic hinge has formed near the corner connection and that the location of the neutral axis has shifted from the beam centerline toward the tension flange. This shift is due to the combined stress state of bending and axial stresses. Each of these observations are expected and lend confidence to the validity of the results. Lastly, it is found that grid refinement from 357 nodes to 621 nodes does not change the simulation results significantly. Figure 9b shows the magnified final (160 kip load) deflected shape for the corner connection. Deflection results without stabilization (Fig. 9a) exhibit hourglass modes in the deformed shape.

Portal Frame

Consider now the response of a portal frame loaded by equal vertical and lateral forces (see Fig. 10). In this case an 8 inch deep I-beam with 4 inch flanges tested by Baker and Rod-

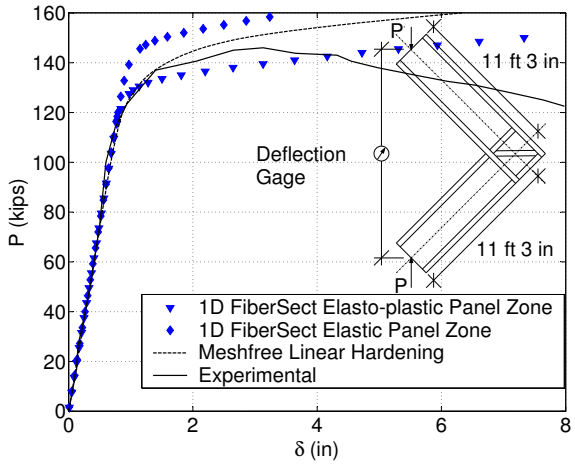

Figure 7: Load displacement response for frame corner connection test.

erick (1952) is utilized in the simulation. Based on the specified web thickness of 1/4 inch, a given plastic moment capacity of 576 k-in and given upper yield stress of 36 ksi provided in Baker and Roderick (1952), the flange thickness is calculated as 0.422 inches. These properties give $Z_x = 16$ in^3 and $I_{xx} = 56.18$ in^4, which are used in the frame analysis. The frame dimensions, support conditions and loading are shown in Fig. 10. Linear hardening is assumed with an assumed ultimate steel stress of 55 ksi. Although the given material was assumed to be A36 steel, the lower yield plateau stress of 33 ksi is used. Load deflection results for a numerical model with 2023 nodes are compared in Fig. 10 to the experimental results provided by Baker and Roderick (1952). The load deflection results are also shown for a 1D fibersection beam model with a discretization of 5 beam elements per column and 10 beam elements for the girder. As the loading progresses hinges develop simultaneously in the beam and column near the top right corner joint of the frame. Following this condition, a constant moment results in the beam segment between the vertical load and the left column. A uniform elasto-plastic stress profile progresses along the beam segment until the frame resists no more load. These observations are consistent with those presented in Baker and Roderick (1952), and the numerical results given here closely match the expected behavior. The load deflection results are in good agreement with the experimental results. Inevitably there are differences between the numerical and experimental results. In addition to this

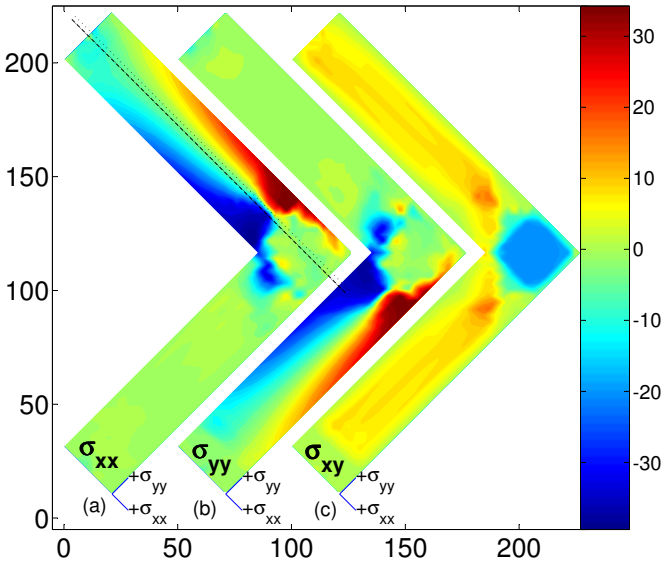

Figure 8: Frame corner connection stresses (ksi): (a) σ_{xx}, (b) σ_{yy} and (c) σ_{xy}

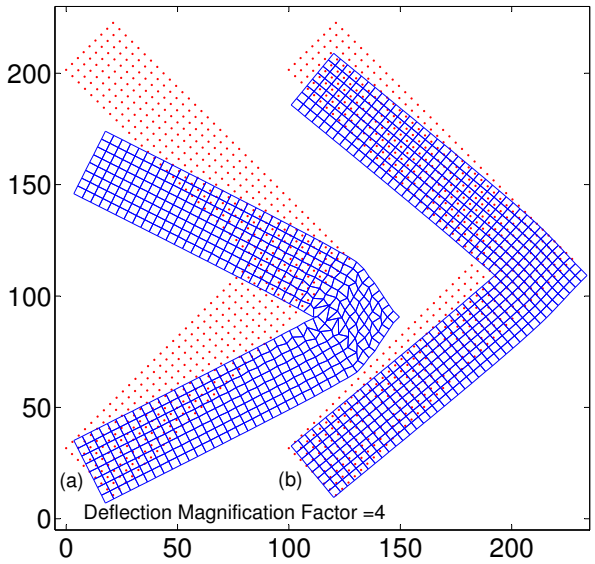

Figure 9: Frame corner connection displacements: (a) without stabilization, (b) with stabilization

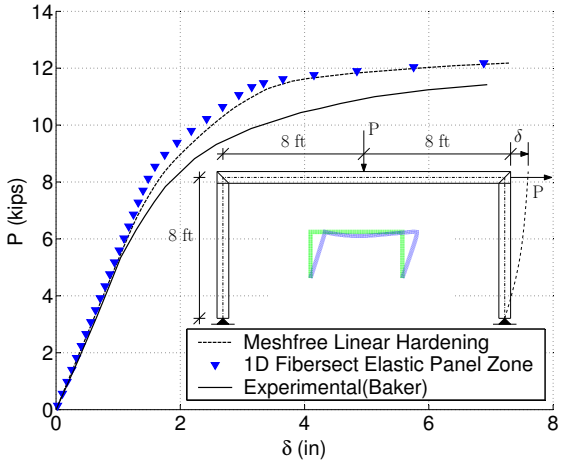

Figure 10: Load deflection plot and test frame setup.

there is always uncertainty in the true material properties of the tested frame as well as uniformity of the quality of welded connections. In fact, Baker and Roderick (1952) state only an assumed yield of 36 ksi and do not provide an estimate for the ultimate stress. Having said this, it is noted that the most important value seems to be the yield stress used in the numerical study. Adjusting ultimate stress and other hardening variables has relatively little affect on the numerical curve shown in Fig. 10. However, using a yield stress of 33 ksi gives numerical results similar to the experiment.

Conclusions

The capabilities of the element-free Galerkin method have been extended in this paper to the inelastic analysis of steel frames. A blended finite element and meshfree method was developed for beam bending approximated as a 2D plane stress problem. The treatment of sections with non-uniform thickness is presented though the particular case of wide-flange sections is considered in the sample simulations. The methodology was applied to solve a variety of frame subassemblies undergoing inelastic deformations. It is shown that the results from the numerical simulations match theory, experimental observations and other finite element based solutions with considerable accuracy. This work has established the feasibility meshfree of methods for the simulation of nonlinear frame response. However, as pointed

out in the introduction, the successful application of meshfree formulation to plane frame analysis is only a first necessary step toward the eventual goal of extending the technology to more complex problems. In this phase of work, only material nonlinearities in a small strain framework were considered. Incorporation of large displacements based on a co-rotational formulation is currently under investigation along with the use of maximum-entropy shape functions (see Sukumar and Wright (2007)) which show promise for easier enforcement of essential boundary conditions and numerical implementation.

Appendix A

In the present work, beams are modeled as a 2D continuum of non-constant thickness in the direction perpendicular to the 2D plane of the domain. For example, in Fig. 11, the Voronoi diagram of a nodal set used to discretize a plane stress cantilever beam domain is shown. In the formulation a thickness, b_f, is specified for the flanges (top and bottom nodes) and a thickness, t_w, for the intermediate nodes of the web (see also Fig. 5c). The specified thickness covers the Voronoi cell area corresponding to each node. As a result the grid spacing defines a grid specific t_f value and one can adjust b_f so the required I_{xx} results. The procedure to accomplish this for an I-section follows. Given an I-beam as shown in

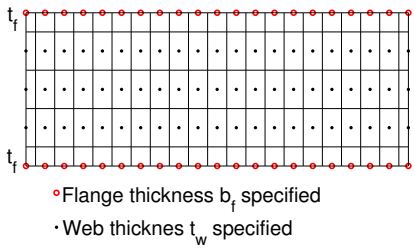

Figure 11: Voronoi diagram.

Fig. 5c, the moment of inertia is written as the sum of contributions from the web and the

flanges. This gives

$$I_w = \frac{t_w(d-2t_f)^3}{12}, \tag{32}$$

$$I_f = \left[2t_f\left(\frac{d-t_f}{2}\right)^2 + \frac{t_f^3}{6}\right] b_f = B_r b_f, \tag{33}$$

where B_r is the coefficient that multiplies b_f in Eq. (33), so that

$$I_{xx} = I_w + I_f. \tag{34}$$

Now, if the grid spacing is arbitrary then t_f is set by the chosen grid. Hence, given I_{xx}, and specified values of t_w and d, the required thickness b_f is obtained as

$$b_f = \frac{I_{xx} - I_w}{B_r}. \tag{35}$$

Equation (35) gives the necessary domain thickness perpendicular to the 2D domain at the flanges. The specific procedure described above can be applied to any cross-section composed of rectangular sections, and, the concept can be extended to fairly arbitrary cross-sections.

Analytical Solution and Comparison to Numerical Results for Elastic I-beam

Using the above procedure for a cantilever I-beam the results of Table 1 are obtained. The numerical analysis and comparison to analytical results proceeds as follows. First, consider the exact analytical elasticity solution for a cantilever beam (see Fig. 5), with transverse shear load at its free end, as discussed in (Timoshenko and Goodier 1951), (Belytschko et al.

1996)

$$u_x = \frac{-Py}{6EI}\left[(6L-3x)x + (2+\nu)\left(y^2 - \frac{D^2}{4}\right)\right] \tag{36a}$$

$$u_y = \frac{P}{6EI}\left[3\nu y^2(L-x) + (4+5\nu)\frac{D^2 x}{4} + (3L-x)x^2\right] \tag{36b}$$

$$\sigma_{xx} = \frac{-P(L-x)y}{I} \tag{36c}$$

$$\sigma_{yy} = 0 \tag{36d}$$

$$\sigma_{xy} = \frac{P}{2I}\left(\frac{D^2}{4} - y^2\right) \tag{36e}$$

where I, which is the moment of inertia for a rectangular cross-section of unit thickness, is given by

$$I = \frac{D^3}{12}. \tag{36f}$$

Even though the solution above is for a *rectangular* beam, it can be applied to I-beams by simply replacing the moment of inertia term, I, in Eqs. (36a-c) by I_{xx}, the moment of inertia for the I-section. Similarly, the moment of inertia of the I-beam web, I_w is used in place of I in Eq. (36e) to determine the shear traction at the right end of the cantilever. The tip displacement solution of the I-beam cantilever is computed from the formula provided by Euler-Bernoulli beam theory with a shear term added, i.e.,

$$\delta_{\text{theoretical}} = \frac{PL^3}{3EI_{xx}} + K\frac{PL}{GA_w}, \tag{37}$$

where $K \approx 1.0$ is typical for I-beams, A_w is the I-beam web area and G is the shear modulus.

Acknowledgments

Helpful discussions with Dr. Michael Puso of Lawrence Livermore National Laboratory are gratefully acknowledged. Research support provided by the National Science Foundation,

through contract grant CMMI-0626481, is also acknowledged.

References

Atluri, S. N., J. Cho, and H. Kim (1999). Analysis of thin beams, using the meshless local Petrov-Galerkin method, with generalized moving least squares interpolations. *Computational Mechanics 2*, 334–347.

Atluri, S. N. and T. Zhu (1998). A new meshless local Petrov-Galerkin (MLPG) approach in computational mechanics. *Computational Mechanics 22*, 117–127.

Baker, J. F. and J. W. Roderick (1952). Tests on full-scale portal frames. *Proceedings of the Institution of Civil Engineers 1*, 71–94. Part 1.

Beedle, L. S. and R. Christopher (1964). Tests of steel moment connections. *AISC Engineering Journal*, 116–125.

Belytschko, T., Y. Krongauz, D. Organ, M. Fleming, and P. Krysl (1996). Meshless methods: an overview and recent developments. *Comput. Methods Appl. Mech. Engrg. 139*, 3–47.

Belytschko, T., Y. Y. Lu, and L. Gu (1994). Element-free Galerkin methods. *International Journal for Numerical Methods in Engineering 37*, 229–256.

Chen, J. S., C. T. Wu, S. Yoon, and Y. You (2001). A stabilized conforming nodal integration for Galerkin meshfree methods. *International Journal for Numerical Methods in Engineering 50*, 435–466.

Chen, J. S., S. Yoon, and C. T. Wu (2002). Non-linear version of stabilized conforming nodal integration for Galerkin mesh-free methods. *International Journal for Numerical Methods in Engineering 53*, 2587–2615.

Donning, B. M. and W. K. Liu (1997). Meshless methods for shear deformable beams and plates. *Comput. Methods Appl. Mech. Engrg. 152*(1–2), 47–71.

Fernández-Méndez, S. and A. Huerta (2004). Imposing essential boundary conditions in mesh-free methods. *Comput. Methods Appl. Mech. Engrg. 193*, 1257–1275.

Fries, T. P. and H. G. Matthies (2004). Classification and overview of meshfree methods. Technical Report Informatikbericht-Nr. 2003-03, Institute of Scientific Computing, Technical University Braunschweig, Braunschweig, Germany.

Gosz, M. R. (2006). *Finite Element Method – Applications in Solids, Structures, and Heat Transfer*. Boca Raton, Florida: CRC Press.

Huerta, A. and S. Fernández-Méndez (2004). A comparison of two formulations to blend finite elements and mesh-free methods. *Comput. Methods Appl. Mech. Engrg. 193*, 1257–1275.

Johnston, B. G., C. H. Yang, and L. S. Beedle (1953). Progress report no. 8, an evaluation of plastic analysis as applied to structural design. *The Welding Journal 32*, 224s–239s. Research Supplement.

Lancaster, P. and K. Salkauskas (1992). Surfaces generated by moving least-squares methods. *Math. Comput. 37*, 141–158.

Li, S. and W. K. Liu (2002). Meshfree and particle methods and their applications. *Appl Mech Rev 55*(1), 1–34.

Liu, W. K., S. Jun, and Y. F. Zhang (1995). Reproducing kernel particle methods. *International Journal for Numerical Methods in Engineering 20*, 1081–1106.

Mazzoni, S., F. McKenna, M. H. Scott, and G. L. Fenves (2007). *OpenSees Command Language Manual*. http://opensees.berkeley.edu/index.php: The Regents of the University of California.

Nayroles, B., G. Touzot, and P. Villon (1992). Generalizing the finite element method: Diffuse appoximation and diffuse elements. *Computational Mechanics 10*, 307–318.

Phillips, A. (1956). *Introduction to Plasticity*. New York: The Ronald Press Co.

Puso, M. A., J. S. Chen, E. Zywicz, and W. Elmer (2008). Meshfree and finite element nodal integration methods. *International Journal for Numerical Methods in Engineering 74*, 416–446.

Simo, J. C. and T. J. R. Hughes (1998). *Computational Inelasticity*. New York: Springer-Verlag.

Simo, J. C. and R. L. Taylor (1986). Return mapping algorithm for plane stress elastoplasticity. *International Journal for Numerical Methods in Engineering 22*, 649–670.

Suetake, Y. (2002). Element-free method based on Lagrange polynomial. *Journal of Engineering Mechanics 128*(2), 231–239.

Sukumar, N. and R. W. Wright (2007). Overview and construction of meshfree basis functions: From moving least squares to entropy approximants. *International Journal for Numerical Methods in Engineering 70*(2), 181–205.

Timoshenko, S. P. and J. N. Goodier (1951). *Theory of Elasticity* (2nd ed.). New York: McGraw-Hill.

Weitzmann, R. (2004). Limit state design of hybrid structures with meshless methods using mathematical optimization. Bauhaus-University Weimar, Institute of Structural Engineering. `http://e-pub.uni-weimar.de/volltexte/2004/7/pdf/M_113.pdf`.

Yu, T. X. and L. C. Zhang (1996). *Plastic Bending - Theory and Applications*. Singapore: World Scientific Publishing.